




Enhanced energy storage and photoluminescence properties in ErBiO₃-doped (Na_{0.5}Bi_{0.5})TiO₃-SrTiO₃ ceramics

Chen Wu¹, Xiaoming Qiu¹, Luyao Chen², Changyi Liu³, Wenxuan Cheng¹, Xiaohu Bing¹, Hongwei Zhao⁴, Wenwei Ge^{1,*} , Zhaodong Liu², and Mingguang Yao²

¹Key Laboratory of Automobile Materials of Ministry of Education, School of Materials Science and Engineering, Jilin University, Changchun 130022, Jilin, China

²State Key Laboratory of Superhard Materials, College of Physics, Jilin University, Changchun 130012, Jilin, China

³Key Laboratory of Bionic Engineering Ministry of Education, Jilin University, Changchun 130025, Jilin, China

⁴School of Mechanical and Aerospace Engineering, Jilin University, Changchun 130025, Jilin, China

Received: 6 September 2021

Accepted: 3 November 2021

Published online:

3 January 2022

© The Author(s), under exclusive licence to Springer Science+Business Media, LLC, part of Springer Nature 2021

ABSTRACT

(1- x)(0.75Na_{0.5}Bi_{0.5}TiO₃-0.25SrTiO₃)- x ErBiO₃ (NBST- x EB, $x = 0$ –0.04) ceramics were fabricated through a solid state reaction method. Scanning electron microscopy investigation shows that grain size of the ceramics decreases with increasing x . X-ray diffraction results reveal that all the ceramics are pseudocubic phase. An enhanced disordering of local structure by EB doping is revealed by Raman spectra. The NBST- x EB ceramics exhibit excellent dielectric stability within a wide temperature range after EB doping. A relatively high recoverable energy storage density (W_{rec}) of 1.834 J/cm³ with efficiency (η) of 71% are obtained for NBST-0.02 EB ceramics under a moderate electric field of 148 kV/cm. The W_{rec} and η of the NBST-0.02 EB ceramics exhibit excellent fatigue stability (10^4) and temperature stability ($W_{\text{rec}} > 0.834$ J/cm³, $\eta > 64\%$) within 30–200 °C under 100 kV/cm. With the introduction of EB, the NBST- x EB ceramics also show strong photoluminescence properties due to the presence of Er³⁺.

Introduction

Dielectric capacitors with fast charge–discharge rates, good durability and temperature stability play an

important role in energy storage applications for micromation of electronic devices [1–8]. The total energy density (W_t), recoverable energy density (W_{rec}) and energy storage efficiency (η) of dielectric

Handling Editor: David Cann.

Address correspondence to E-mail: wenweige@jlu.edu.cn

<https://doi.org/10.1007/s10853-021-06704-5>

capacitors can be calculated according to Eqs. (1)–(3) [3, 4]

$$W_t = \int_0^{P_{\max}} E dP \quad (1)$$

$$W_{\text{rec}} = \int_{P_r}^{P_{\max}} E dP \quad (2)$$

$$\eta = W_{\text{rec}}/W \times 100\% \quad (3)$$

where E and P are electric field and polarization which can be obtained from the P - E hysteresis loops. P_r and P_{\max} are remnant polarization and maximum induced polarization under a given E . In order to get a high W_{rec} and η , materials having slim P - E hysteresis loops with large P_{\max} and small P_r are preferred. In normal ferroelectrics (FEs), large P_{\max} often accompanies with large P_r , which results in small value in W_{rec} and η . However, relaxor ferroelectrics (RFEs) with short range ordered polar nano-regions (PNRs) show large P_{\max} and small P_r simultaneously [9]. So the RFEs are considered to be ideal base materials for designing high performance electrical energy storage materials in recent years. For environmental concern, $\text{Na}_{0.5}\text{Bi}_{0.5}\text{TiO}_3$ (NBT) lead-free perovskite with complex ions occupying on its A-site attracts much attention because it can form solid solutions with many other lead-free perovskites, such as $\text{SrNb}_{0.5}\text{Sc}_{0.5}\text{O}_3$ (SNS) [10], $\text{SrNb}_{0.5}\text{Al}_{0.5}\text{O}_3$ (SNA) [11], NaTaO_3 (NT) [12] and SrTiO_3 (ST) [13–17]. The energy storage performance of pure NBT ceramics is poor because of the low dielectric break down strength (E_b) and large P_r . For dielectric ceramics, there are many strategies to improve E_b based on different breakdown processes [8, 18]. First, increasing band gap or phonon frequency. Large band gap can limit the electrons from the valence band to the conduction band and high phonon frequency means a quick energy loss rate [8]. Second, decreasing average grain size (AGS). The grain boundary regions will increase with decreasing AGS and a higher resistivity can be obtained because the grain boundaries can act as barriers to trap charge carriers [8, 18]. In addition, decreasing AGS can result in the pore size become small, which leads to a reduction of the local voltage applied on the pore and reduces the possibility of dielectric breakdown [8]. Third, inhibiting defects. Defects, such as impurities, pores, vacancies and so on, are always difficult to avoid during ceramic processing, especially in NBT ceramics because its A-site elements are volatile

during sintering processing [19]. Compared with matrix material, the area containing defects usually exhibits a lower withstand voltage. Therefore, inhibiting defects is an effective way to improve E_b . Generally, by incorporating some chemical compounds, the E_b can be significantly enhanced in NBT ceramics at the expense of decreasing P_{\max} due to the negative correlation between dielectric permittivity (ϵ_r) and E_b [8]. However, although P_{\max} is destroyed, these compounds not only can disturb long range ferroelectric order to generate PNRs leading to a decreasing P_r , but also can decrease the dielectric nonlinearity or delay the polarization saturation of NBT ceramics [8]. Therefore, by compound doping, the excellent energy storage properties (ESPs) can be achieved under a high E in NBT-based ceramics. For example, high W_{rec} of 6.64 J/cm^3 and 4.21 J/cm^3 were reported for 0.8NBT-0.2SNA ceramics and 0.8NBT-0.2NT ceramics under an extremely high E of 520 kV/cm [11] and 380 kV/cm [12], respectively.

The requirement of ultra-high E might be a handicap for the practical device applications [20, 21]. NBT- x ST solid solution ceramics possess pinched P - E loops with large P_{\max} , small P_r and enhanced E_b ($\sim 100 \text{ kV/cm}$) at the ST content of 24–28 mol% [13–17]. By introducing the third component to form ternary solid solutions, enhanced (W_{rec} , η) of (2.03 J/cm^3 , 61.8%) and (1.746 J/cm^3 , 71%) were obtained for 0.76NBT-0.24ST-AgNbO₃ and 0.72NBT-0.28ST-BiAlO₃ ceramics under a moderate $E = 120 \text{ kV/cm}$ [13, 17]. By defect engineering with Bi-excess and Na-deficiency to compensate the volatilization of Bi during sintering, enhanced E_b and reduced P_r can be obtained without sacrifice of P_{\max} in 0.75Bi_(0.5+x)-Na_(0.5-x)TiO₃-0.25ST ceramics when the x is less than 0.02. Because of high electrical resistivity, the rare earth oxide Er₂O₃ is often used to enhance the E_b for ferroelectric ceramics [22–24]. Moreover, because of the special energy level of Er³⁺, Er³⁺-doped NBT-based ceramics show strong photoluminescence (PL) properties exhibiting strong green emission at $\sim 550 \text{ nm}$ and red emission at $\sim 660 \text{ nm}$ [25]. In addition, the PL intensity is usually used to value the PL properties [26], which is affected by many factors mainly including the concentration of Er³⁺, composition of matrix material, defects and so on [27]. Furthermore, it was reported that enhanced relaxor characteristics and refined grain size were obtained in K_{0.5}Na_{0.5}NbO₃ (KNN) ceramics via the doping of complex oxide 0.5Er₂O₃-0.5Bi₂O₃ (or ErBiO₃,

abbreviated as EB hereafter), which leads to transparent ceramics with enhanced energy storage performance and PL properties [28, 29]. Inspired by these results, EB were chosen as a modifier for 0.75NBT-0.25ST ceramics in this work to realize the enhancement of E_b without significant decrease in P_{max} under a moderate E . Our results demonstrate that the (W_{recr}, η) can be enhanced from (0.703 J/cm³, 45%) to (0.961 J/cm³, 63%) for 0.75NBT-0.25ST ceramics after 1 mol% EB doping under 100 kV/cm. The E_b of 148 kV/cm and (W_{recr}, η) of (1.834 J/cm³, 71%) were obtained after 2 mol% EB doping. Besides the enhanced ESPs, PL properties were also enhanced after EB doping, which makes EB-doped 0.75NBT-0.25ST a potential multifunctional material for electrical and optical applications.

Experimental procedure

$(1-x)(0.75Na_{0.5}Bi_{0.5}TiO_3-0.25SrTiO_3)-xErBiO_3$ (NBST- x EB) ceramics were fabricated through a solid state reaction method. Raw materials of TiO_2 ($\geq 98\%$), Bi_2O_3 ($\geq 99\%$), Na_2CO_3 ($\geq 99.8\%$), $SrCO_3$ ($\geq 99\%$) and Er_2O_3 ($\geq 99.9\%$) were dried at 120 °C for 2 h. Then the raw materials were weighed according to the mole ratio of $x = 0, 0.01, 0.02, 0.03$ and 0.04 . The mixed raw materials were ball milled for 1 h with alcohol. After ball milling, the mixed raw materials were dried and calcined at 900 °C for 3 h to obtain ceramic powders. Then the ceramic powders were ground and ball milled for 8 h. After ball milling, the ceramic powders were pressed into pellets with dimensions of $\Phi 10\text{ mm} \times 1\text{ mm}$ under a cold isostatic pressure of 250 MPa. Finally, these pellets were sintered at 1150–1200 °C for 2 h.

The sintered ceramics were polished with parallel surfaces and silver electrodes were fired on both parallel surfaces at 600 °C for 0.5 h. Temperature dependent dielectric properties were measured by using a DMS-500 (Partulab). In order to measure the ferroelectric properties under high E , gold electrodes were sputtered on the polished parallel surfaces of the samples with a small upper electrode and a large bottom electrode. The small electrode was obtained by using 3.00 mm mask during sputtering process. The large electrode ($\sim 9\text{ mm}$) was sputtered on the surface of the samples without the mask. The P – E loops were measured at 10 Hz with a Precision LC II (Radiant Technologies Inc, USA). Microstructures

of the NBST- x EB ceramics were observed by a scanning electron microscopy (SEM, Magellan 400, FEI, USA) equipped with an energy dispersive spectrometer (EDS, Max150, Oxford-X, UK). X-ray diffraction (XRD) data were measured by using a Rigaku D/max-2500/PC system. Lattice vibration related with local structures of the NBST- x EB ceramics were measured by using a Raman spectrometer (LabRAM HR Evolution Raman) with a 473 nm exciting laser. The Raman spectra were taken on three spots for each composition and error analyses were performed. In addition, the Raman spectrometer was used to collect the photoluminescence spectra.

Results and discussion

SEM micrographs and grain size distribution of the NBST- x EB ceramics are shown in Fig. 1a–e. Inhomogeneous grain size can be seen for the NBST ceramics in Fig. 1a. After doping of EB, the grain size distribution become uniform and all the ceramics exhibit a dense microstructure without obvious pores. The secondary phases with lamellar structure is present in the micrographs for $x \geq 0.02$, which could be the Bi-rich phase as evidenced in our following XRD results. Except for the Bi-rich phase region, the results of SEM–EDS demonstrate NBST-0.02 EB ceramics have good chemical uniformity as shown in Fig. 1h–j. With increasing x , average grain size (AGS) of NBST- x EB ceramics decreases from 1.99 μm to 1.30 μm for $x = 0$ and 0.01 and continues to decrease for $x = 0.02$, as shown in Fig. 1f. Then the average grain size slightly increases for $x = 0.03$ and 0.04. After doping EB, part of Er and Bi ions might enter perovskite A-site, which compensates the volatilization of Na and Bi in NBST and reduce the concentration of oxygen vacancies. The increasing atomic mass on the A-site and decreasing concentration of oxygen vacancies will hinder substance and energy transfer across grain boundary during sintering process, which results in the reduced AGS in EB-doped NBST ceramics [19]. The reduced AGS is beneficial to enhancement of E_b due to high density of grain boundary which acts as barriers to trap more charge carriers [22].

XRD patterns of NBST- x EB ceramics are shown in Fig. 2a. Pure perovskite phases are found for NBST- x EB ceramics with $x = 0$ and 0.01. Additional

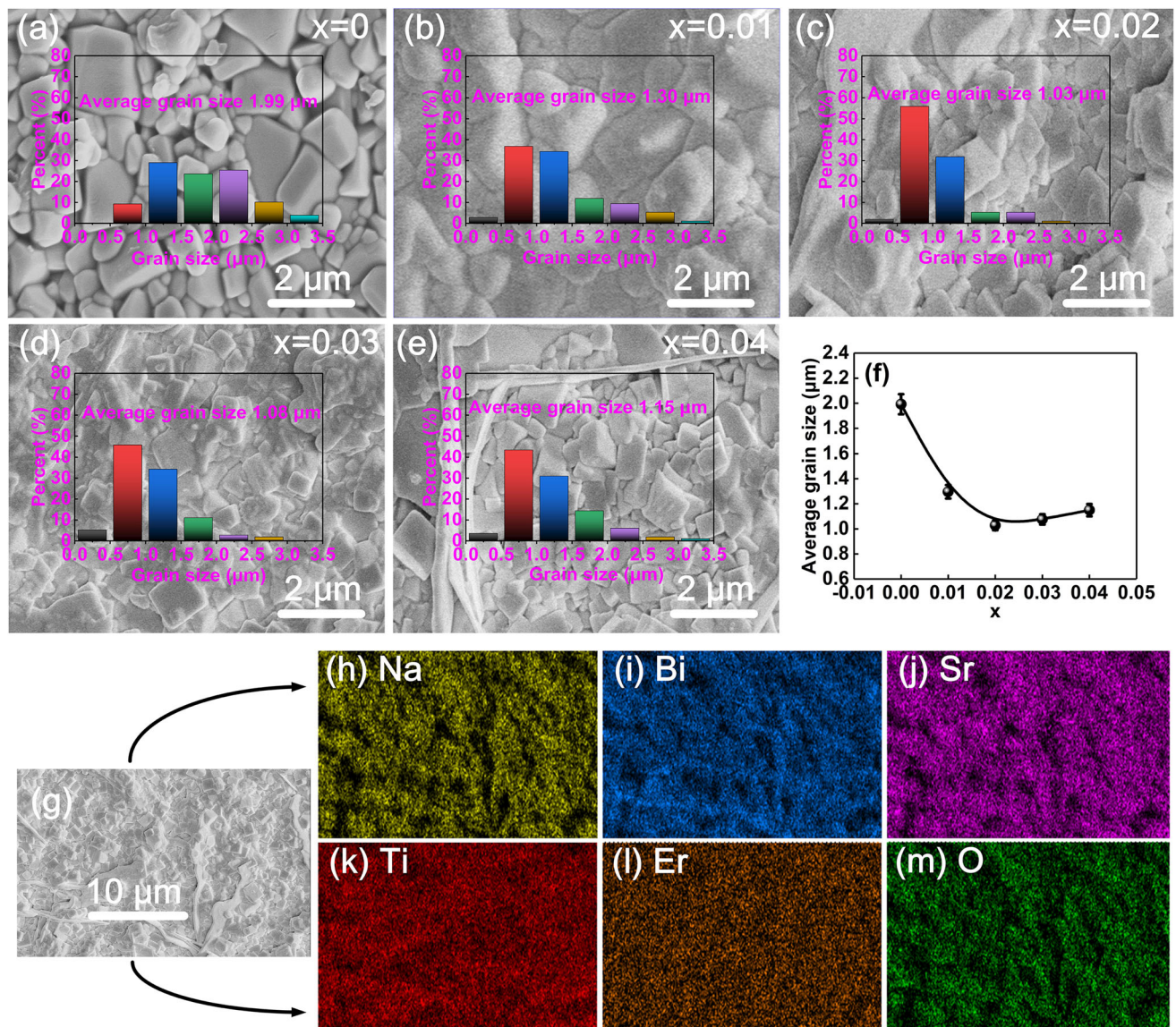


Figure 1 The SEM images of NBST- x EB ceramics: **a** $x = 0$, **b** $x = 0.01$, **c** $x = 0.02$, **d** $x = 0.03$ and **e** $x = 0.04$. Insets are the grain size distribution corresponding to respective bulk ceramics.

f The average grain size as function of EB content. **g–m** The microstructure and corresponding EDS mapping images for NBST-0.02 EB ceramics.

diffraction peaks corresponding to $\text{Bi}_2\text{Ti}_2\text{O}_7$ phase exist for $x = 0.02$ – 0.04 , which might be the secondary phase as observed by the SEM results. (111) and (200) diffraction peaks which are referred to a perovskite cubic lattice are magnified in Fig. 2b, c. There is no obvious splitting for both (111) and (200) diffraction peaks, which indicates the perovskite phases of NBST- x EB ceramics are close to cubic structure or so called pseudocubic structure in literatures [14, 15]. With increasing x , the 2θ of (111) and (200) peaks shift toward higher angle direction because unit cell becomes smaller when the smaller Er^{3+} enters into

the A-site of perovskite. Effects of EB doping on the local structure are revealed by Raman spectra, as shown in Fig. 3a. According to the vibration mode, the Raman spectra of NBST- x EB can be divided into four regions corresponding to A-site vibration (100 – 200 cm^{-1}), B–O bond vibration (200 – 400 cm^{-1}), BO_6 octahedral vibration (400 – 700 cm^{-1}) and $\text{A}_1 + \text{E}$ vibration (700 – 900 cm^{-1}) [14], which can be deconvoluted into eight Lorentz peaks as represented in Fig. 3a for NBST-0.04 EB ceramics. Raman shift, integrated intensity and full width at half maximum (FWHM) as functions of x for the deconvoluted peaks

Figure 2 The XRD patterns of NBST- x EB ceramics in the 2θ range of **a** 20–80°, **b** 39–41°, **c** 45.5–47.5°.

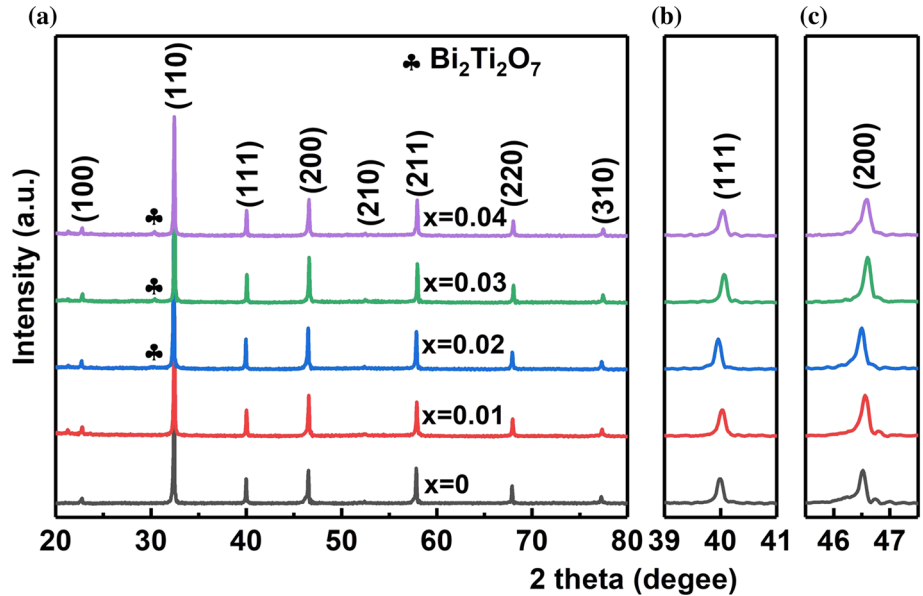
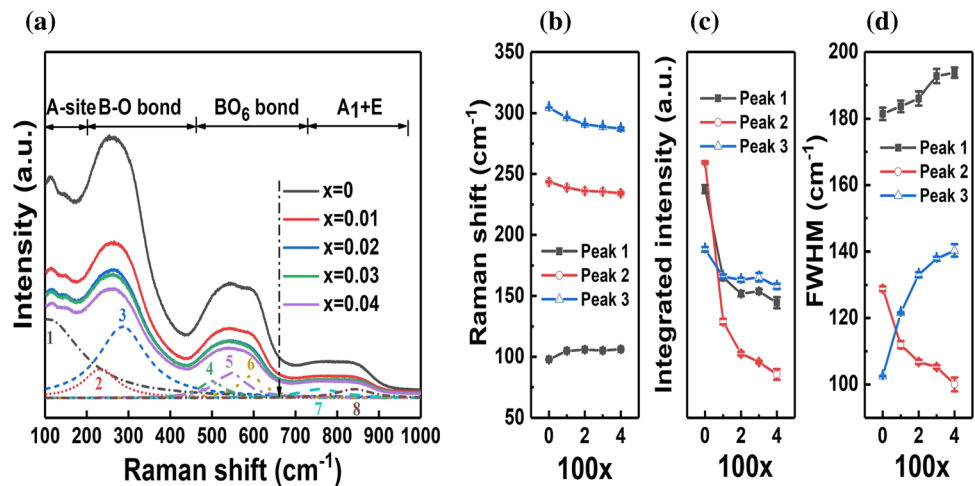


Figure 3 **a** Raman spectra of the NBST- x EB ceramics and representative deconvoluted results for the NBST-0.04 EB ceramics. **b–d** Raman shift, integrated intensity and FWHM as functions of EB content x for peaks 1, 2 and 3.



corresponding to the A-site and B-O bond vibrations are shown in Fig. 3b, d. All the three parameters of Raman spectra monotonically change with increasing x , which clearly indicates that Er^{3+} and Bi^{3+} are incorporated into perovskite lattice of NBST ceramics. The B–O bond vibration is closely related to the structure and dielectric properties of NBT-based materials [14, 30–32], which are deconvoluted into peak 2 and 3. With increasing x , the Raman shift of peaks 2 and 3 gradually shifts toward low wavenumber, indicating the softening of the Ti–O vibrations mirroring the de-coupling of the Ti–O bonds [30]. Considering the polarity of NBT-based ceramics is mainly originated from the strong coupling of the Bi–O and Ti–O bonds [33], therefore, the de-coupling of the Ti–O bonds will lead to the

descending dielectric and ferroelectric properties. The integrated intensities of the peaks 1, 2 and 3 monotonically decrease with increasing x , which implies that the perovskite structure changes gradually toward a cubic one as evidenced by XRD in Fig. 2b, c. The FWHM of peak 1 increases with increasing x , which might provide an experimental evidence that the disordering on the A-site are enhanced due to Er^{3+} entering the A-site. The broadened and diffused Raman spectra indicate enhanced disordering of local structures in NBST- x EB ceramics after EB doping [14, 30–32].

Figure 4a–e shows the temperature dependent dielectric permittivity (ϵ_r) and loss factor ($\tan\delta$) for NBST- x EB ceramics under various frequencies. Below 150 °C, a strong frequency dispersion can be

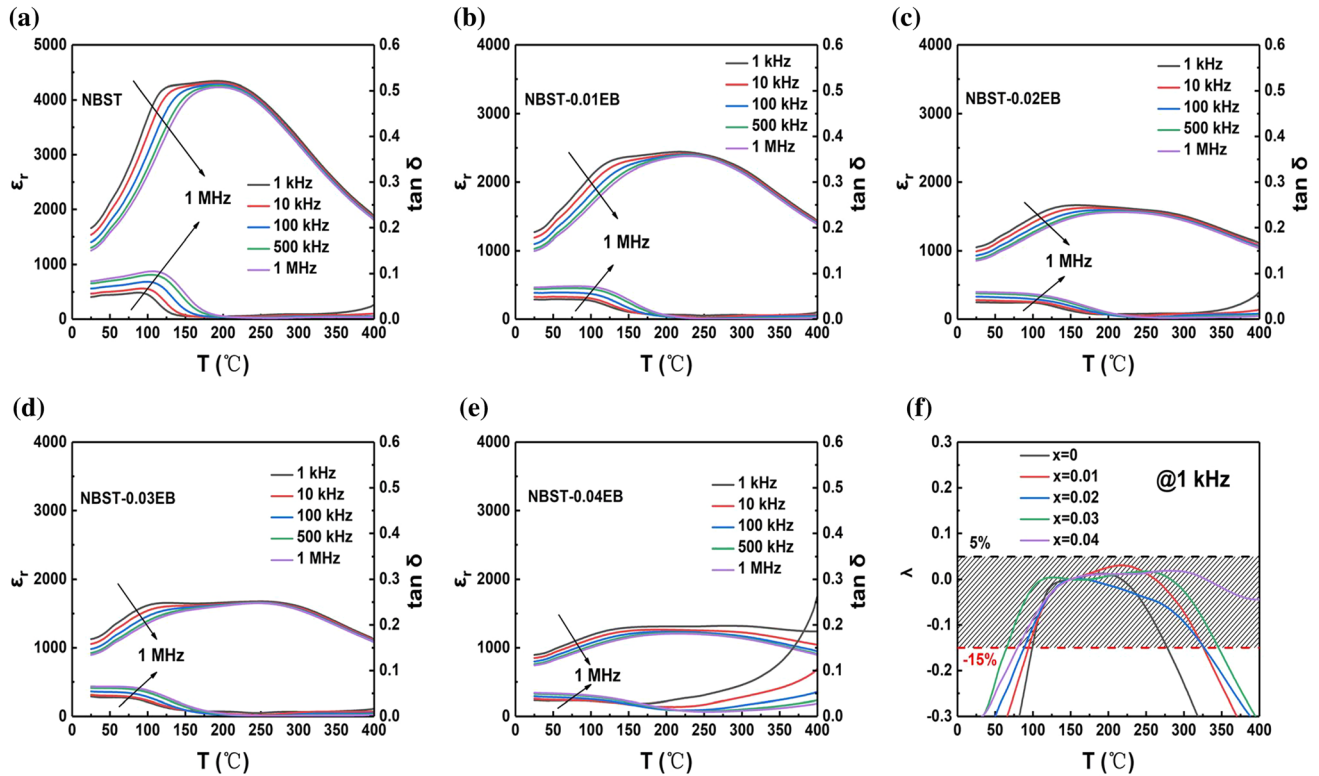


Figure 4 The dielectric constant (ϵ_r) and loss factor ($\tan\delta$) as functions of temperature for NBST- x EB ceramics under different frequencies: **a** $x = 0$, **b** $x = 0.01$, **c** $x = 0.02$, **d** $x = 0.03$ and **e** $x = 0.04$. (f) The λ – T curves of NBST- x EB ceramics at 1 kHz.

seen on both ϵ_r and $\tan\delta$ for NBST ceramics. The temperature corresponding to the dielectric peaks within the frequency dispersion range increases with increasing frequency, which shows some similarity with that of typical relaxor ferroelectrics [34, 35]. The ϵ_r decreases significantly with EB doping, which can be attributed to the weakening Ti–O bonds as evidenced by the Raman spectra. In addition, the frequency dispersion shows two different features. First, the temperature range of frequency dispersion slightly extends to high temperature. Second, the temperature corresponding to the dielectric peak gradually becomes frequency independent and merged into a very broad dielectric platform with increasing x to 0.04. $\lambda = (\epsilon_{r,T} - \epsilon_{r,150^\circ\text{C}}) / \epsilon_{r,150^\circ\text{C}}$ is often used to describe the temperature stability of high-temperature dielectric capacitors because 150 °C is a benchmark operating temperature [36–38]. Figure 4f shows the λ as a function of temperature (T) for NBST- x EB ceramics at 1 kHz and the shaded area represents the λ value between 5 and –15%. $\epsilon_{r,150^\circ\text{C}}$, $\tan\delta_{150^\circ\text{C}}$ and T (–15% < λ < 5%) of NBST- x EB ceramics at 1 kHz are collected in Table 1. The temperature stability range are broadened by EB doping

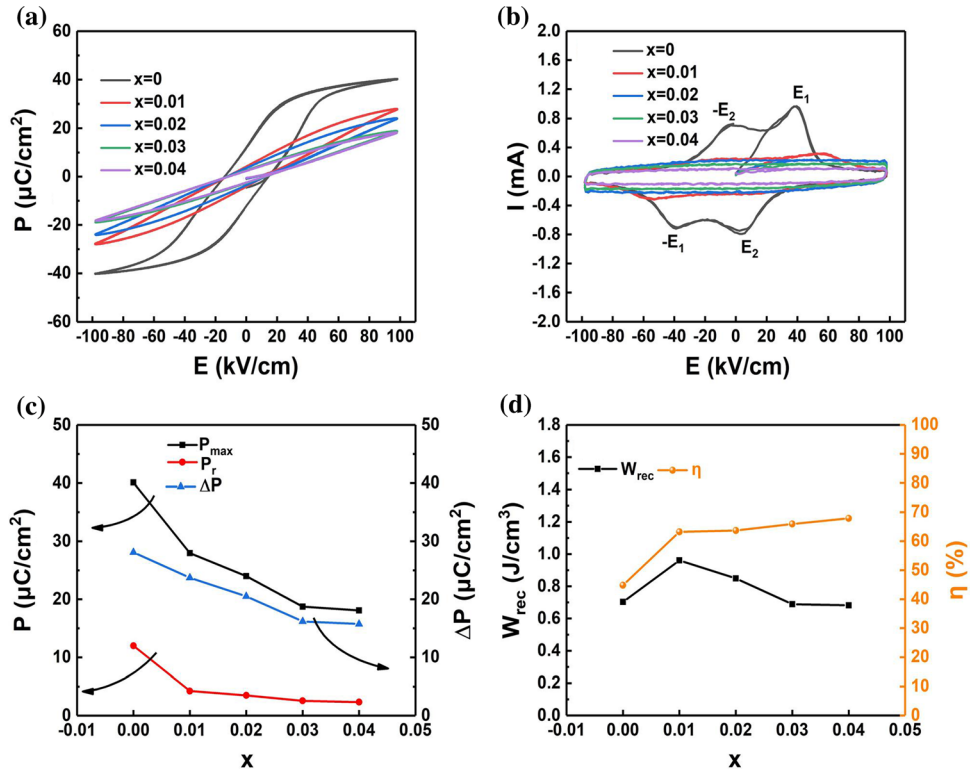
in NBST ceramics and all the ceramics have a high $\epsilon_{r,150^\circ\text{C}}$ (> 1290) and low $\tan\delta_{150^\circ\text{C}}$ (< 0.03). Therefore, NBST- x EB ceramics can be used as potential high-temperature dielectric capacitor materials.

Figure 5a, b shows the P – E loops and switching current (I)– E loops measured at room temperature under 100 kV/cm for NBST- x EB ceramics. The P – E loops become slimmer as EB content increases. P_{max} , P_r and $\Delta P = P_{\text{max}} - P_r$ gradually decrease with increasing EB content, as shown in Fig. 5c. These results indicate that doping EB can disturb long-

Table 1 The values of $\epsilon_{r,150^\circ\text{C}}$, $\tan\delta_{150^\circ\text{C}}$ and T (–15% < λ < 5%) of NBST- x EB ceramics at 1 kHz

Compositions	$\epsilon_{r,150^\circ\text{C}}$	$\tan\delta_{150^\circ\text{C}}$	T (–15% < λ < 5%)
$x = 0$	4286.8	0.0089	99–277 °C
$x = 0.01$	2369.8	0.0161	94–325 °C
$x = 0.02$	1659.3	0.0185	88–327 °C
$x = 0.03$	1648.8	0.0133	64–345 °C
$x = 0.04$	1295.9	0.0283	78–400 °C

Figure 5 **a** The P - E loops of NBST- x EB ceramics under 100 kV/cm. **b** The I - E loops of NBST- x EB ceramics under 100 kV/cm. **c** P_{\max} , P_r and ΔP as functions of EB content. **d** W_{rec} and η as functions of EB content.



range ferroelectric ordering in NBST ceramics and enhance the disordering of the local structures as evidenced by the Raman spectra in Fig. 3. Four peaks ($\pm E_1$ and $\pm E_2$) on the I - E loops are seen for NBST ceramics in Fig. 5b. The peaks occurring at $\pm E_1$ indicate the E induced phase transition from RFE to FE, while the reversible transition from FE phase to RFE occurs at $\pm E_2$ [36]. With increasing EB content, the $\pm E_1$ peaks gradually fade, which indicates RFE is maintained without long range ordered FE induced under 100 kV/cm. Figure 5d shows the W_{rec} and η calculated according to Eqs. (1–3) for NBST- x EB ceramics under 100 kV/cm. The (W_{rec}, η) of NBST ceramics can be enhanced from (0.703 J/cm³, 45%) to (0.961 J/cm³, 63%) by 1 mol% EB doping. The improvement of (W_{rec}, η) is as high as (37%, 40%). With further increasing x , the W_{rec} decreases while the η increases slightly.

Unipolar P - E loops were measured for the NBST- x EB ceramics before breakdown, as displayed in Fig. 6a. The highest (W_{rec}, η) of (1.834 J/cm³, 71%) are obtained for NBST-0.02 EB ceramics under a maximum E_b of 148 kV/cm. The excellent ESPs obtained at $x = 0.02$ which can be attributed two factors: one is the enhanced E_b due to the refined grain size and enhanced electrical resistivity by EB doping [22–24];

another important factor is the enhanced disordering of the local structures as evidenced by the Raman spectra in Fig. 3. The enhanced disordering of the local structures might generate nanodomains and PNRs [35]. Compared with large-scale ferroelectric domains, these nanodomains and PNRs not only can be aligned under a given E , but also can back to its original state when E is unloaded [8]. Therefore, for $x = 0.02$, a relatively large P_{\max} and small P_r can be obtained under 148 kV/cm. However, nanodomains and PNRs might be further refined and even eliminated with increasing x , which leads to a significantly reduced P_{\max} under a given E [39]. Therefore, although the enhanced E_b is also obtained for $x = 0.03$ and 0.04, the W_{rec} of 1.457 J/cm³ and 1.421 J/cm³ are relatively lower than that of $x = 0.02$ due to a small P_{\max} . The comparison of W_{rec} between NBST-0.02 EB ceramics and recently reported NBT-based ceramics is shown in Fig. 6c [10, 40–49]. It can be seen that the W_{rec} of NBST-0.02 EB ceramics possesses a considerable advantage under a relatively low E .

Figure 7a, b shows the temperature dependent P - E loops and (W_{rec}, η) for NBST-0.02 EB ceramics from 30 to 200 °C under 100 kV/cm. The P - E loops gradually become linear as temperature increases. (W_{rec}, η) increase from (0.834 J/cm³, 64%) to (0.967 J/cm³,

Figure 6 **a** The unipolar P - E loops of NBST- x EB ceramics before breakdown. **b** The corresponding W_{rec} and η as functions of EB content. **c** The comparison of W_{rec} between NBST-0.02 EB ceramics and recently reported NBT-based ceramics.

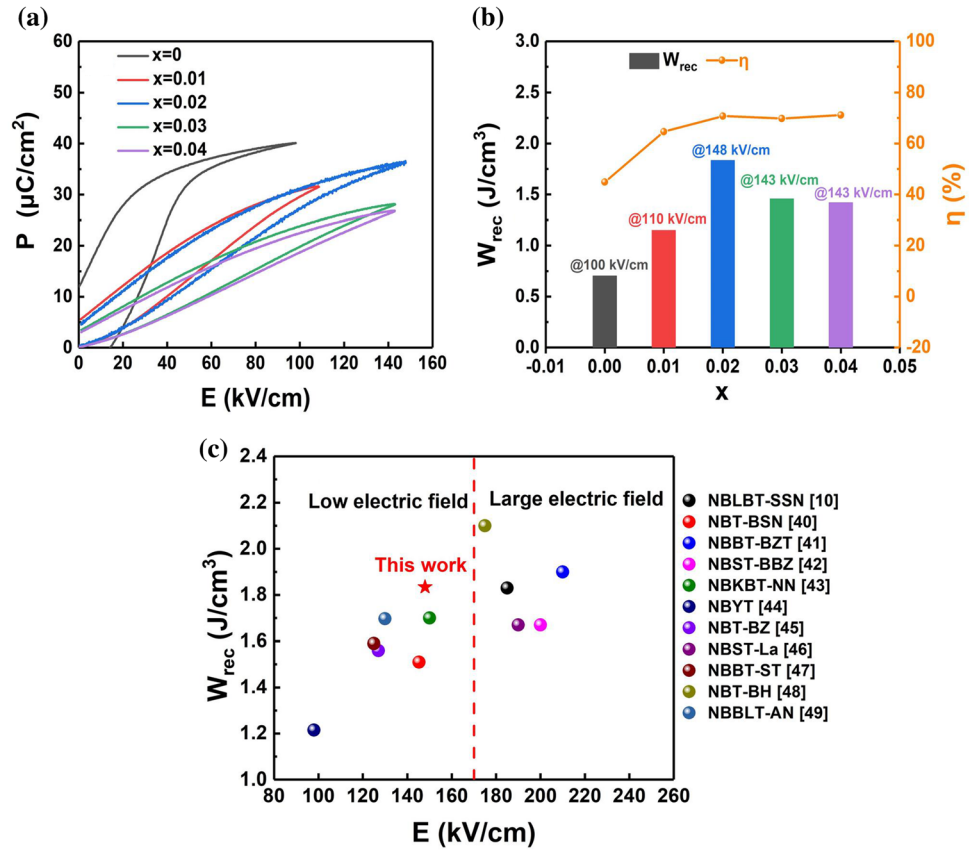


Figure 7 **a** and **b** the temperature stability of NBST-0.02 EB ceramics from 30 to 200 °C under 100 kV/cm. **c** and **d** the fatigue stability of NBST-0.02 EB ceramics from 1 to 10⁴ under 100 kV/cm.

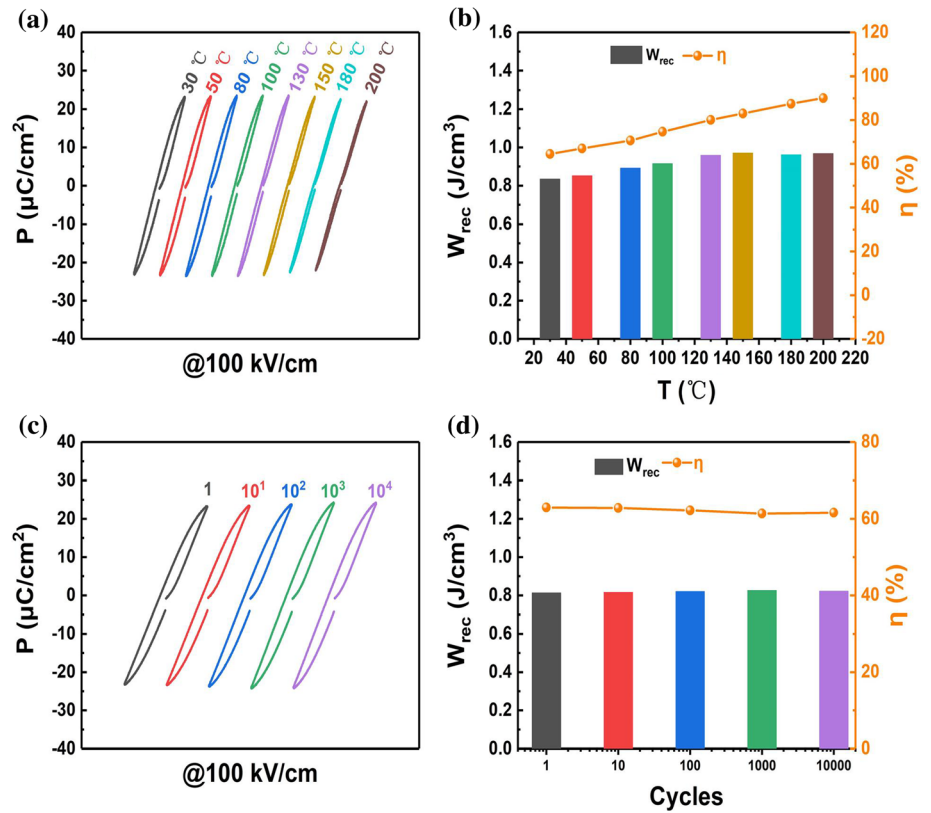
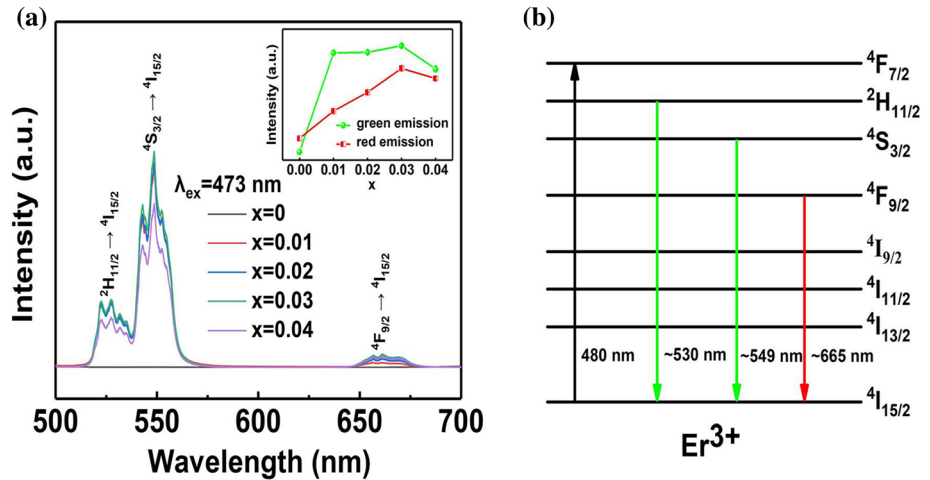


Figure 8 **a** The photoluminescence spectra of NBST-*x*EB ceramics. The inset shows the green and red emission intensities as functions of EB content. **b** The energy level scheme of Er³⁺ ion.



90%) with increasing temperature from 30 to 200 °C. These results demonstrate that ESPs of NBST-0.02 EB ceramics exhibit excellent temperature stability within temperature range of 30–200. Figure 7c, d displays the *P*–*E* loops and (*W*_{rec}, *η*) of NBST-0.02 EB ceramics with the loaded cycles from 1 to 10⁴ under 100 kV/cm. It can be seen that the *P*–*E* loops are almost unchanged from 1 to 10⁴ cycles. The variations of *W*_{rec} and *η* are only 1.19% and 2.16%, indicating excellent fatigue stability of ESPs for NBST-0.02 EB ceramics.

Photoluminescence (PL) properties of NBST-*x*EB ceramics are shown in Fig. 8a. NBST ceramics does not show any PL properties. After EB doping, NBST-*x*EB ceramics exhibit two green emissions (²H_{11/2} → ⁴I_{15/2} at ~ 530 nm and ⁴S_{3/2} → ⁴I_{15/2} at ~ 549 nm) and one red emission (⁴F_{9/2} → ⁴I_{15/2} at ~ 665 nm) excited under 473 nm light, which is similar to the previously reported results in Er-doped NBT-based ceramics [25, 50]. The mechanism of PL properties for EB-doped ceramics can be well illustrated by the energy level scheme of Er³⁺ ion, as shown in Fig. 8b. The electrons located at the ground state (⁴I_{15/2}) can be excited to ⁴F_{7/2} level upon 473 nm light excitation, then these electrons can quickly relax to ²H_{11/2}, ⁴S_{3/2} and ⁴F_{9/2} levels by nonradiative manner due to the small energy gaps and unstable ⁴F_{7/2} level [25]. Finally, most of them recombine and back to the ground state (⁴I_{15/2}) leading to two green emissions (²H_{11/2} → ⁴I_{15/2} at ~ 530 nm and ⁴S_{3/2} → ⁴I_{15/2} at ~ 549 nm) and one red emission (⁴F_{9/2} → ⁴I_{15/2} at ~ 665 nm) [25]. The variations for emission intensities of the wavelength at 549 nm (green) and 665 nm (red) with EB content are shown

in an inset of Fig. 8. The green and red emission intensities increase and reach a maximum value at *x* = 0.03, then decrease with further increasing of *x* which might result from concentration quenching of Er³⁺ [51].

Conclusions

This study reveals that EB is an effective structure and property modifier for the NBST ceramics. The grain size can be refined by EB doping. Cation disordering on the A-site of perovskite is enhanced while the distortion from cubic structure is reduced with increasing EB content. Therefore, the *P*_r can be significantly decreased by EB doping. The relatively high *W*_{rec} of 1.834 J/cm³ and *η* of 71% under a moderate *E* of 148 kV/cm are obtained for NBST-0.02 EB ceramics, exhibiting excellent temperature (30–200 °C) and fatigue stabilities (10⁴) under 100 kV/cm. Moreover, with the EB doping, all ceramics show strong PL properties. Thus, the NBST-*x*EB ceramics can be considered as potential electric-optical multifunctional materials.

Acknowledgements

This work was supported by the Fundamental Research Funds for the Central Universities JLU under 1018320174002, by the Provincial Natural Science Foundation of Jilin under Grant No. 20200201097JC, and by the National Natural Science Foundation of China under Grants No. 52032012 and 52172004.

Data availability statement

The datasets generated during the current study are available from the corresponding author on reasonable request.

Declarations

Conflict of interest The authors declare that they have no conflict of interest.

References

- [1] Sun ZX, Wang Z, Tian Y, Wang G, Wang W, Yang MD, Wang XY, Zhang FH, Pu YP (2019) Progress, outlook, and challenges in lead-free energy-storage ferroelectrics. *Adv Electron Mater* 6:1900698. <https://doi.org/10.1002/aelm.201900698>
- [2] Li F, Zhai JW, Shen B, Zeng HR (2019) Recent progress of ecofriendly perovskite-type dielectric ceramics for energy storage applications. *J Adv Dielectr* 08:1830005. <https://doi.org/10.1142/s2010135x18300050>
- [3] Yang LT, Kong X, Li F, Hao H, Cheng ZX, Liu HX, Li JF, Zhang SJ (2019) Perovskite lead-free dielectrics for energy storage applications. *Prog Mater Sci* 102:72–108. <https://doi.org/10.1016/j.pmatsci.2018.12.005>
- [4] Yao ZH, Song Z, Hao H, Yu ZY, Cao MH, Zhang SJ, Lanagan MT, Liu HX (2017) Homogeneous/inhomogeneous-structured dielectrics and their energy-storage performances. *Adv Mater* 29:1601727. <https://doi.org/10.1002/adma.201601727>
- [5] Zhang X, Hu D, Pan ZB, Lv XJ, He ZY, Yang F, Li P, Liu JJ, Zhai JW (2021) Enhancement of recoverable energy density and efficiency of lead-free relaxor-ferroelectric BNT-based ceramics. *Chem Eng J* 406:126818. <https://doi.org/10.1016/j.cej.2020.126818>
- [6] Liu G, Li Y, Guo B, Tang MY, Li Q, Dong J, Yu LJ, Yu K, Yan Y, Wang DW, Zhang LY, Zhang HB, He ZB, Jin L (2020) Ultrahigh dielectric breakdown strength and excellent energy storage performance in lead-free barium titanate-based relaxor ferroelectric ceramics via a combined strategy of composition modification, viscous polymer processing, and liquid-phase sintering. *Chem Eng J* 398:125625. <https://doi.org/10.1016/j.cej.2020.125625>
- [7] Yang ZT, Du HL, Jin L, Hu QY, Wang H, Li YF, Wang JF, Gao F, Qu SB (2019) Realizing high comprehensive energy storage performance in lead-free bulk ceramics via designing an unmatched temperature range. *J Mater Chem A* 7:27256. <https://doi.org/10.1039/c9ta11314b>
- [8] Yang ZT, Du HL, Jin L, Poelman D (2021) High-performance lead-free bulk ceramics for electrical energy storage applications: design strategies and challenges. *J Mater Chem A* 9:18026. <https://doi.org/10.1039/d1ta04504k>
- [9] Cross LE (1987) Relaxor ferroelectrics. *Ferroelectrics* 76:241–267. <https://doi.org/10.1080/00150198708016945>
- [10] Xie JL, Dai ZH, Ding XD, Fan X, Liu WG, Zhang L, Li JL (2020) Enhanced energy storage properties of Sr(Sc_{0.5}Nb_{0.5})O₃ modified (Bi_{0.47}La_{0.03}Na_{0.5})_{0.94}Ba_{0.06}TiO₃ lead-free ceramics. *J Mater Sci* 55:13578–13589. <https://doi.org/10.1007/s10853-020-04978-9>
- [11] Yan F, Zhou XF, He X, Bai HR, Wu SH, Shen B, Zhai JW (2020) Superior energy storage properties and excellent stability achieved in environment-friendly ferroelectrics via composition design strategy. *Nano Energy* 75:105012. <https://doi.org/10.1016/j.nanoen.2020.105012>
- [12] Zhou XF, Qi H, Yan ZN, Xue GL, Luo H, Zhang D (2019) Superior thermal stability of high energy density and power density in domain-engineered Bi_{0.5}Na_{0.5}TiO₃-NaTaO₃ relaxor ferroelectrics. *ACS Appl Mater Interfaces* 11:43107–43115. <https://doi.org/10.1021/acsami.9b13215>
- [13] Ma W, Zhu Y, Marwat MA, Fan P, Xie B, Salamon D, Ye Z-G, Zhang H (2019) Enhanced energy-storage performance with excellent stability under low electric fields in BNT–ST relaxor ferroelectric ceramics. *J Mater Chem C* 7:281–288. <https://doi.org/10.1039/c8tc04447c>
- [14] Li F, Zhai JW, Shen B, Liu X, Yang K, Zhang Y, Li P, Liu BH, Zeng HR (2017) Influence of structural evolution on energy storage properties in Bi_{0.5}Na_{0.5}TiO₃-SrTiO₃-NaNbO₃ lead-free ferroelectric ceramics. *J Appl Phys* 121:054103. <https://doi.org/10.1063/1.4975409>
- [15] Zhu Y, Zhang YY, Xie B, Fan PY, Marwat MA, Ma WG, Wang C, Yang B, Xiao JZ, Zhang HB (2018) Large electric field-induced strain in AgNbO₃-modified 0.76Bi_{0.5}Na_{0.5}TiO₃-0.24SrTiO₃ lead-free piezoceramics. *Ceram Int* 44:7851–7857. <https://doi.org/10.1016/j.ceramint.2018.01.220>
- [16] Liu G, Dong J, Zhang LY, Yan Y, Jing RY, Jin L (2020) Phase evolution in (1-x)(Na_{0.5}Bi_{0.5})TiO₃-xSrTiO₃ solid solutions: a study focusing on dielectric and ferroelectric characteristics. *J Mater Sci* 6:677–691. <https://doi.org/10.1016/j.jmat.2020.05.005>
- [17] Shi P, Zhu LG, Gao WW, Yu ZH, Lou XJ, Wang XJ, Yang ZM, Yang S (2019) Large energy storage properties of lead-free (1-x)(0.72Bi_{0.5}Na_{0.5}TiO₃-0.28SrTiO₃)-xBiAlO₃ ceramics at broad temperature range. *J Alloy Compd* 784:788–793. <https://doi.org/10.1016/j.jallcom.2019.01.077>
- [18] Wang G, Lu ZL, Li Y, Li LH, Ji HF, Feteira A, Zhou D, Wang DW, Zhang SJ, Reaney IM (2021) Electroceramics for high-energy density capacitors: current status and future

- perspectives. *Chem Rev* 121:6124–6172. <https://doi.org/10.1021/acs.chemrev.0c01264>
- [19] Yan F, Huang KW, Jiang T, Zhou XF, Shi YJ, Ge GL, Shen B, Zhai JW (2020) Significantly enhanced energy storage density and efficiency of BNT-based perovskite ceramics via A-site defect engineering. *Energy Storage Mater* 30:392–400. <https://doi.org/10.1016/j.ensm.2020.05.026>
- [20] Zhang L, Pu YP, Chen M, Zhuo FP, Dietz C, Frömling T (2021) Decreasing polar-structure size: achieving superior energy storage properties and temperature stability in $\text{Na}_{0.5}\text{Bi}_{0.5}\text{TiO}_3$ -based ceramics for low electric field and high-temperature applications. *J Eur Ceram Soc* 41:5890–5899. <https://doi.org/10.1016/j.jeurceramsoc.2021.05.036>
- [21] Kang RR, Wang ZP, Lou XJ, Liu WY, Shi P, Zhu XP, Guo XD, Li SY, Sun HN, Zhang LX, Sun QZ (2021) Energy storage performance of $\text{Bi}_{0.5}\text{Na}_{0.5}\text{TiO}_3$ -based relaxor ferroelectric ceramics with superior temperature stability under low electric fields. *Chem Eng J* 410:128376. <https://doi.org/10.1016/j.ccej.2020.128376>
- [22] Zhao P, Tang B, Fang ZX, Si F, Yang CT, Zhang SR (2021) Improved dielectric breakdown strength and energy storage properties in Er_2O_3 modified $\text{Sr}_{0.35}\text{Bi}_{0.35}\text{K}_{0.25}\text{TiO}_3$. *Chem Eng J* 403:126290. <https://doi.org/10.1016/j.ccej.2020.126290>
- [23] Cao L, Yuan Y, Li EZ, Zhang SR (2019) Improvement of dielectric breakdown strength and energy storage performance in Er_2O_3 -modified $0.95\text{Sr}_{0.7}\text{Ba}_{0.3}\text{Nb}_2\text{O}_6-0.05\text{CaTiO}_3$ lead-free ceramics. *Ceram Int* 45:5660–5667. <https://doi.org/10.1016/j.ceramint.2018.12.031>
- [24] Shen ZY, Hu QG, Li YM, Wang ZM, Luo WQ, Hong Y, Xie ZX, Liao RH (2013) Structure and dielectric properties of $\text{Re}_{0.02}\text{Sr}_{0.97}\text{TiO}_3$ (Re = La, Sm, Gd, Er) ceramics for high-voltage capacitor applications. *J Am Ceram Soc* 96:2551–2555. <https://doi.org/10.1111/jace.12364>
- [25] Du P, Luo LH, Li WP, Zhang YP, Chen HB (2013) Electrical and luminescence properties of Er-doped $\text{Bi}_{0.5}\text{Na}_{0.5}\text{TiO}_3$ ceramics. *Mater Sci Eng B-Adv Funct Solid-State Mater* 178:1219–1223. <https://doi.org/10.1016/j.mseb.2013.08.007>
- [26] Hu B, Pan Z, Dai M, Guo FF, Ning HP, Gu ZB, Chen J, Lu MH, Zhang ST, Yang B, Cao WW (2014) Photoluminescence and temperature dependent electrical properties of Er-doped $0.94\text{Bi}_{0.5}\text{Na}_{0.5}\text{TiO}_3-0.06\text{BaTiO}_3$ ceramics. *J Am Ceram Soc* 97:3877–3882. <https://doi.org/10.1111/jace.13217>
- [27] Li KX, Luo LH, Zhang YY, Li WP, Hou YF (2018) The upconversion luminescence modulation and its enhancement in Er^{3+} -doped $\text{Na}_{0.5}\text{Bi}_{0.5}\text{TiO}_3$ based on photochromic reaction. *J Am Ceram Soc* 101:5640–5650. <https://doi.org/10.1111/jace.15879>
- [28] Xing J, Huang YL, Wu B, Liu HG, Tan Z, Chen Q, Zhang W, Xiao DQ, Zhu JG (2020) Energy storage behavior in ErBiO_3 -doped (K, Na) NbO_3 lead-free piezoelectric ceramics. *ACS Appl Electron Mater* 2:3717–3727. <https://doi.org/10.1021/acsaelm.0c00745>
- [29] Lin C, Wu X, Lin M, Huang YP, Li J (2017) Optical, luminescent and optical temperature sensing properties of $(\text{K}_{0.5}\text{Na}_{0.5})\text{NbO}_3\text{-ErBiO}_3$ transparent ceramics. *J Alloy Compd* 706:156–163. <https://doi.org/10.1016/j.jallcom.2017.02.245>
- [30] Fu J, Zuo RZ (2013) Giant electrostrains accompanying the evolution of a relaxor behavior in $\text{Bi}(\text{Mg}, \text{Ti})\text{O}_3\text{-PbZrO}_3\text{-PbTiO}_3$ ferroelectric ceramics. *Acta Mater* 61:3687–3694. <https://doi.org/10.1016/j.actamat.2013.02.055>
- [31] Jiang XJ, Wang BY, Luo LH, Li WP, Zhou J, Chen HB (2014) Electrical properties of $(1-x)(\text{Bi}_{0.5}\text{Na}_{0.5})\text{TiO}_3-x\text{KNbO}_3$ lead-free ceramics. *J Solid State Chem* 213:72–78. <https://doi.org/10.1016/j.jssc.2014.01.022>
- [32] Kreisel J, Glazer AM, Bouvier P, Lucazeau G (2001) High-pressure raman study of a relaxor ferroelectric: the $\text{Na}_{0.5}\text{Bi}_{0.5}\text{TiO}_3$ perovskite. *Phys Rev B* 63:174106. <https://doi.org/10.1103/PhysRevB.63.174106>
- [33] Schutz D, Deluca M, Krauss W, Feteira A, Jackson T, Reichmann K (2012) Lone-pair-induced covalency as the cause of temperature- and field-induced instabilities in bismuth sodium titanate. *Adv Funct Mater* 22:2285–2294. <https://doi.org/10.1002/adfm.201102758>
- [34] Phelan D, Stock C, Rodriguez-Rivera JA, Chi SX, Leao J, Long XF, Xie YJ, Bokov AA, Ye ZG, Ganesh P, Gehring PM (2014) Role of random electric fields in relaxors. *Proc Natl Acad Sci U S A* 111:1754–1759. <https://doi.org/10.1073/pnas.1314780111>
- [35] Shvartsman VV, Lupascu DC (2012) Lead-free relaxor ferroelectrics. *J Am Ceram Soc* 95:1–26. <https://doi.org/10.1111/j.1551-2916.2011.04952.x>
- [36] Qiao XS, Sheng AH, Wu D, Zhang FD, Chen B, Liang PF, Wang JJ, Chao XL, Yang ZP (2021) A novel multifunctional ceramic with photoluminescence and outstanding energy storage properties. *Chem Eng J* 408:127368. <https://doi.org/10.1016/j.ccej.2020.127368>
- [37] Benyoussef M, Zannen M, Belhadi J, Manoun B, Dellis JL, El Marssi M, Lahmar A (2018) Dielectric, ferroelectric, and energy storage properties in dysprosium doped sodium bismuth titanate ceramics. *Ceram Int* 44:19451–19460. <https://doi.org/10.1016/j.ceramint.2018.07.182>
- [38] Liu Y, Li YL, Zheng ZS, Kang WS, Xi KB, Mi YS (2021) Dielectric temperature stability of Nb-modified $\text{Bi}_{0.5}(\text{Na}_{0.78}\text{K}_{0.22})_{0.5}\text{TiO}_3$ lead-free ceramics. *Ceram Int* 47:4933–4936. <https://doi.org/10.1016/j.ceramint.2020.10.067>

- [39] Ye HR, Yang F, Pan ZB, Hu D, Lv XJ, Chen HX, Wang FF, Wang JS, Li P, Chen JW, Liu JJ, Zhai JW (2021) Significantly improvement of comprehensive energy storage performances with lead-free relaxor ferroelectric ceramics for high-temperature capacitors applications. *Acta Mater* 203:116484. <https://doi.org/10.1016/j.actamat.2020.116484>
- [40] Fan ZH, Yu YX, Huang J, Zhang QF, Lu YM, He YB (2021) Excellent energy storage properties over a wide temperature range under low driving electric fields in NBT-BSN lead-free relaxor ferroelectric ceramics. *Ceram Int* 47:4715–4721. <https://doi.org/10.1016/j.ceramint.2020.10.040>
- [41] Fan XM, Li P, Du JA, Chen C, Fu P, Hao JG, Yue ZX, Li W (2020) High-energy storage performance of $(1-x)0.935(\text{Bi}_{0.5}\text{Na}_{0.5})\text{TiO}_3-0.065\text{BaTiO}_3-x\text{Ba}(\text{Zr}_{0.3}\text{Ti}_{0.7})\text{O}_3$ ceramics with wide temperature range. *J Mater Sci-Mater Electron* 31:9974–9981. <https://doi.org/10.1007/s10854-020-03602-5>
- [42] Liu G, Wang Y, Han GY, Gao JH, Yu LJ, Tang MY, Li Y, Hu JZ, Jin L, Yan Y (2020) Enhanced electrical properties and energy storage performances of NBT-ST Pb-free ceramics through glass modification. *J Alloy Compd* 836:154961. <https://doi.org/10.1016/j.jallcom.2020.154961>
- [43] Liu XD, Hou YD, Xu YR, Zheng MP, Zhu MK (2020) Realization of temperature insensitive high energy storage performance via introducing NaNbO_3 into NBT-KBT system. *J Alloy Compd* 844:156163. <https://doi.org/10.1016/j.jallcom.2020.156163>
- [44] Yan BB, Fan HQ, Wang C, Zhang MC, Yadav AK, Zheng XK, Wang H, Du ZN (2020) Giant electro-strain and enhanced energy storage performance of $(\text{Y}_{0.5}\text{Ta}_{0.5})^{4+}$ co-doped $0.94(\text{Bi}_{0.5}\text{Na}_{0.5})\text{TiO}_3-0.06\text{BaTiO}_3$ lead-free ceramics. *Ceram Int* 46:281–288. <https://doi.org/10.1016/j.ceramint.2019.08.261>
- [45] Yu YX, Zhang YY, Zhang Y, Li H, Zhang QF, Lu YM, He YB (2020) High-temperature energy storage performances in $(1-x)(\text{Na}_{0.50}\text{Bi}_{0.50}\text{TiO}_3)-x\text{BaZrO}_3$ lead-free relaxor ceramics. *Ceram Int* 46:28652–28658. <https://doi.org/10.1016/j.ceramint.2020.08.024>
- [46] Yao K, Zhou CR, Wang J, Tan YC, Li QN, Yuan CL, Xu JW, Rao GH (2021) $\text{Bi}_{0.5}\text{Na}_{0.5}\text{TiO}_3-\text{Sr}_{0.85}\text{Bi}_{0.1}\text{TiO}_3$ ceramics with high energy storage properties and extremely fast discharge speed via regulating relaxation temperature. *Ceram Int* 47:11294–11303. <https://doi.org/10.1016/j.ceramint.2020.12.255>
- [47] Wang H, Yuan H, Liu X, Wu KY, Zheng QJ, Xu CG, Lin DM (2021) Achieving high energy-storage properties in $\text{Bi}_{0.5}\text{Na}_{0.5}\text{TiO}_3$ -based lead-free ceramics under low electric fields. *Ceram Int* 47:1344–1352. <https://doi.org/10.1016/j.ceramint.2020.08.256>
- [48] Zhang L, Pu YP, Chen M, Wei TC, Keipper W, Shi RK, Guo X, Li R, Peng X (2020) High energy-storage density under low electric fields and improved optical transparency in novel sodium bismuth titanate-based lead-free ceramics. *J Eur Ceram Soc* 40:71–77. <https://doi.org/10.1016/j.jeurceramsoc.2019.09.001>
- [49] Wang H, Jiang XL, Liu XQ, Yang RN, Yang Y, Zheng QJ, Kwok KW, Lin DM (2019) An effective approach to achieve high energy storage density and efficiency in BNT-based ceramics by doping AgNbO_3 . *Dalton Trans* 48:17864–17873. <https://doi.org/10.1039/c9dt03654g>
- [50] Chen C, Xia X, Zheng LQ, Luo LH, Tu N, Shen ZY, Jiang XP, Liu JM (2019) Effects of phase structure on up-conversion photoluminescence and dielectric performance in Er^{3+} doped $(\text{Bi}_{0.5}\text{Na}_{0.5})\text{TiO}_3-\text{BaTiO}_3$ lead-free ceramics. *J Alloy Compd* 801:619–625. <https://doi.org/10.1016/j.jallcom.2019.06.147>
- [51] Pan HL, Zhang JJ, Jia XR, Xing HJ, He JY, Wang JY, Wen F (2018) Large electrostrictive effect and high optical temperature sensing in $\text{Bi}_{0.5}\text{Na}_{0.5}\text{TiO}_3-\text{BaTiO}_3-(\text{Sr}_{0.7}\text{Bi}_{0.18}\text{Er}_{0.02})\text{TiO}_3$ luminescent ferroelectrics. *Ceram Int* 44:5785–5789. <https://doi.org/10.1016/j.ceramint.2017.12.067>

Publisher's Note Springer Nature remains neutral with regard to jurisdictional claims in published maps and institutional affiliations.